ELSEVIER

PII: S0032-3861(97)10256-7

Polymer Vol. 39 No. 25, pp. 6315–6324, 1998

0032-3861/98/$ - see front matter

Development of toughness in ABS resins

G. F. Giaconi[a], L. Castellani[b,*], C. Maestrini[b] and T. Riccò[a]
[a]*Department of Materials Engineering, University of Trento, Via Mesiano 77, 38050 Trento, Italy*
[b]*EniChem Research Centre, Via Taliercio 14, 46100 Mantova, Italy*
(Received 23 December 1996; revised 28 April 1997; accepted 13 October 1997)

Different ABS systems, produced by means of different polymerisation techniques (emulsion and mass polymerisations) and with different microstructural features were characterised and studied. Elastoplastic fracture mechanics tests were performed in order to compare the effects of the different morphologies of the dispersed phase on the mechanical responses. The plastic deformation mechanisms that give rise to energy dissipation were investigated in situ by means of transmission electron microscopy, and correlated to the observed fracture properties. Information about the stress field around and inside the dispersed particles was also obtained by dynamic mechanical analysis. The microstructural characteristics of the materials account well for the performance differences: particles from emulsion polymerisation, in particular, can cavitate and then promote plastic deformation through shear yielding.

(Keywords: ABS; toughening mechanisms; fracture mechanics of toughened plastics)

INTRODUCTION

Acrylonitrile–styrene–butadiene (ABS) polymers have great market relevance: they are used from the appliance to the car industries because of their good properties balance: these materials, in fact, represent a valuable compromise in mechanical, aesthetic and processing properties.

ABS is formed by a matrix of random styrene–acrylonitrile (SAN) copolymer in which a population of approximately spherical rubbery particles, generally made of polybutadiene (PB) and having sizes in a range from 0.05 to 5 μm, is dispersed: the adhesion between the matrix and the second phase is provided by some graft SAN–PB copolymer at the interfaces. The presence of the rubbery particles is the reason for the improved toughness of ABS: SAN is in fact quite a brittle material, whose critical stress intensity factor, K_c, is not far from that of polystyrene (PS), being close to about 1–2 MPa·m$^{1/2}$.

The mechanisms of rubber toughening have been widely examined in recent years and it is evident that the augmented toughness is obtained when the second phase is able to trigger and amplify on a microscopic scale the matrix plastic deformation mechanisms. Furthermore, the presence of the second phase can modify the stress–strain state of the matrix, changing its microdeformation modes from less to more energy consuming ones: in ABS, for example, this happens when the deformation balance goes from *crazing* to *shear yielding*. Because of this, it is evident that the amount, dimensions, structure and properties of the second rubbery phase are extremely relevant in the assessment of the ABS macroscopic mechanical performance. Therefore, knowledge and control of these parameters allow ABS producers to tailor their products according to the applications. This possibility is increased by the fact that ABS can also be produced by mass polymerisation processes[1], beside the traditional ABS emulsion polymerisation. In fact, the two different polymerisation processes give rise to rubbery particles whose structure is fairly different.

The aim of this work is to analyse and compare from a complete mechanical point of view, i.e. considering both the macroscopic performance and the microscopic plastic mechanisms, some ABSs produced by the two different polymerisation techniques.

EXPERIMENTAL

Materials

ABS materials produced by emulsion polymerisation and by mass polymerisation, henceforth referred to as E and M, respectively, were considered for the present investigations. A substantial difference in the internal structure of the rubbery phase particles obtained by the two processes is apparent from the TEM micrographs in *Figure 1*: emulsion-made ABS has bulk rubber particles, with almost no sub-included SAN; conversely, mass polymerised materials have, inside the dispersed particles, a high included SAN content, with a 'salami' morphology similar to that of conventional high impact polystyrene (HIPS).

For each of the two internal particles structures, samples with different particle sizes and size distributions were chosen: samples E1 and E2 have small and large particles, respectively, and samples M1, M2 and M3 have increasing particle size, with a particularly large particle size distribution for sample M3.

In addition, a pure SAN copolymer was selected in order to prepare, by extrusion blending with the ABS materials, diluted samples having various levels of second phase content. The molecular characteristics of the SAN sample were chosen to be similar to those of the matrices of the ABS samples.

Table 1 reports the relevant composition and molecular weight data of the five undiluted ABS samples. Emulsion-made samples have a high PB content and a high amount of insoluble phase (separation of the insoluble phase was carried out according to the procedure reported in Refs 2 and 3): this

* To whom correspondence should be addressed

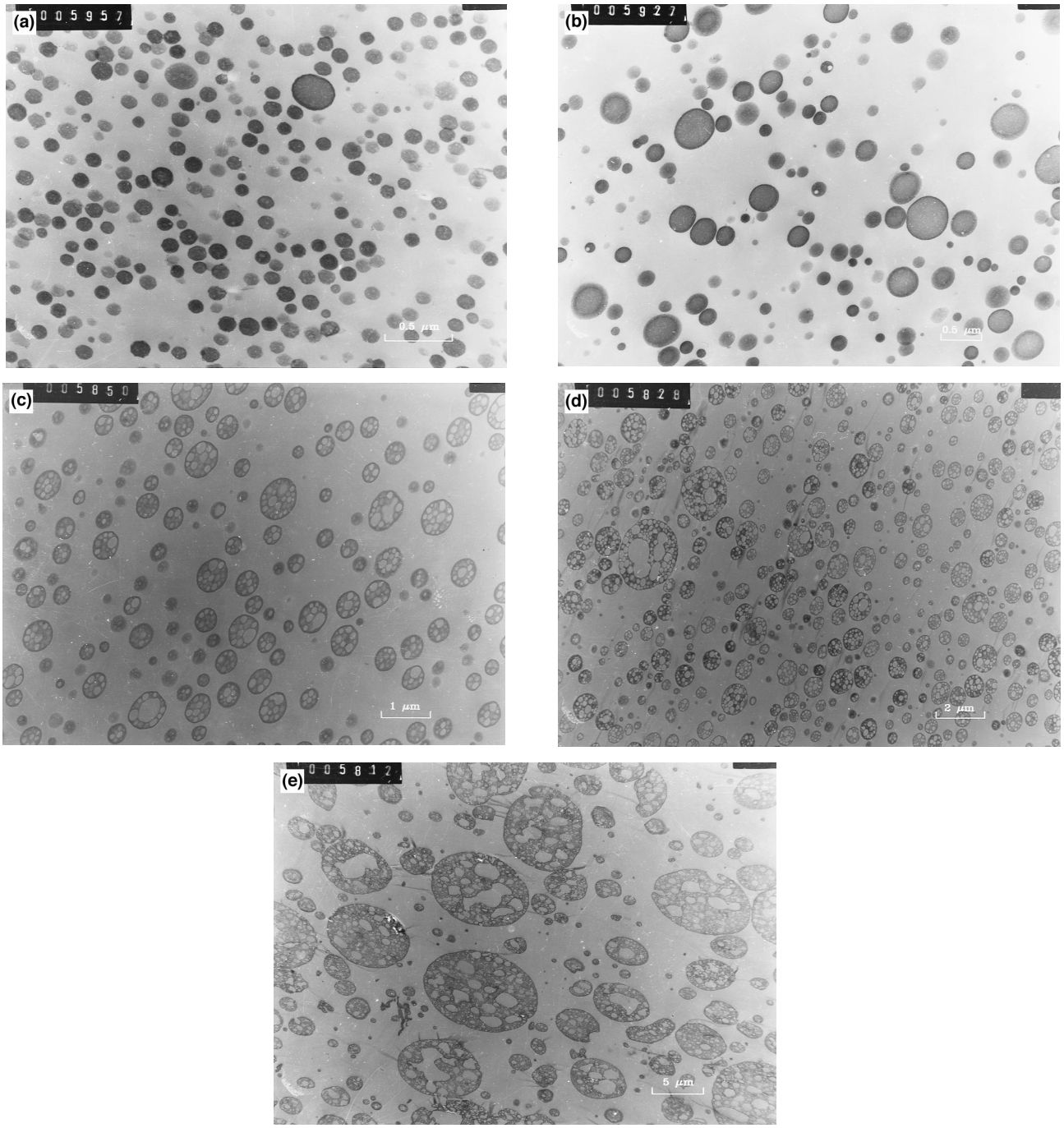

Figure 1 TEM micrographs of the five ABS samples: (a) E1/10; (b) E2/10; (c) M1; (d) M2; (e) M3

shows that most of the SAN in these materials is grafted to the cross-linked PB particles. Mass polymerised samples, however, have a much lower PB content and a considerable amount of ungrafted SAN, as indicated by the low amount of insoluble phase. No data are reported in *Table 1* concerning the key characteristics of the rubbery phase, that is the total second phase content and the particle size distributions. Reliable measurement of these parameters is not easy, especially when comparing samples with different morphologies, and the issue is addressed in the following section.

Diluted samples, obtained from each ABS by mixing with SAN as described above, were prepared to have 5, 10, 15 and 20 wt% of insoluble phase for the mass polymerised materials and 5, 10, 15 and 20 wt% of PB for the emulsion

Table 1 Characteristics of the materials

	Material				
	E1	E2	M1	M2	M3
PB (wt%)	49.0	67.5	11.0	10.8	10.9
ST (wt%)	37.5	24.0	65.0	65.5	66.3
AN (wt%)	11.5	7.8	23.2	23.2	22.7
AN/SAN (%)	23.4	24.5	26.3	26.1	25.5
Matrix M_w	121 000	103 000	145 000	118 000	107 000
Matrix M_w/M_n	3.5	4.3	2.4	2.5	2.1
Insoluble phase content	90.2	87.2	19.2	19.2	19.6

materials (*Table 1*). In the cases of M1, M2 and M3 the highest concentration samples were obtained by simply extruding, with no added SAN, the original ABS, their insoluble phase content being close to 20%.

Five series of samples were thus available for the mechanical characterisation, each of them corresponding to one of the five different rubbery-phase morphologies, and each constituted by four samples having different insoluble phase content. In the following, samples are identified by a letter related to the polymerisation process, followed by a number corresponding to the particle size and by a second number indicating the dilution level (e.g. M1/10 is the mass polymerised sample with the smallest particle size, diluted to an insoluble phase content of 10 wt%; E2/15 is the emulsion sample with large particles at a PB content of 15 wt%).

Microstructural characterisation

In order to realise a really precise and quantitatively useful structural characterisation, an accurate determination of the particle size distribution and of the rubbery phase volume fraction is necessary. The materials were analysed by a standard separation technique according to the procedure described in Refs 2 and 3. However, the value of the second phase volume fraction that one obtains from this separation technique (indicated as ϕ_{sep} in the following) is subject to some criticism and gives rise to data that cannot be considered realistic[3].

Recently one of us proposed a stereological approach which is described in detail in Ref. 3 and which consists of analysing transmission electron microscopy (TEM) pictures, obtained following the standard technique reported in Ref. 3, from material slices having different thickness and then reconstructing the bulk situation. The model uses the following equations:

$$\langle r^1\rangle = \frac{\pi\langle R^2\rangle + 2t\langle R^1\rangle}{4\langle R^1\rangle + 2t}, \tag{1}$$

$$\langle r^2\rangle = \frac{4\langle R^3\rangle + 3t\langle R^2\rangle}{6\langle R^1\rangle + 3t}, \tag{2}$$

$$\phi_{app} = \frac{4\langle R^3\rangle + 3t\langle R^2\rangle}{4\langle R^3\rangle}, \tag{3}$$

where $\langle r^i\rangle$ represents the ith moment of the particle radius distribution in the TEM images, $\langle R^j\rangle$ the jth moment of the real particle distribution in the bulk, t the observed section thickness, ϕ_{app} the apparent second phase volume fraction in the TEM images and ϕ the real second phase volume fraction.

Table 2 Morphological parameters of the considered materials

	Material				
	E1/10	E2/10	M1	M2	M3
$\langle R^1\rangle$ (μm)	0.050	0.084	0.131	0.211	0.665
$\langle R^2\rangle$ (μm^2)	0.0026	0.0089	0.0281	0.0623	0.442
$\langle R^3\rangle$ (μm^3)	0.0002	0.0012	0.0056	0.0208	0.592
σ	0.000	0.043	0.104	0.133	0.000*
ϕ (%)	9.7	10.9	16.8	23.8	41.2
Sub-inclusion (%)			37	56	73
ϕ_{sep} (%)	10.0	10.0	19.2	19.2	19.6

The meaning of the symbols is illustrated in the text. The SAN sub-inclusion volume fraction in the particles (sub-inclusion %) is simply computed from ϕ and the PB content (%) (*Table 1*) values. The datum indicated with an asterisk is questionable (see text). Data relative to ϕ_{sep} of E materials correspond to the pure PB content

Equations (1)–(3), which produce an over-determined system when one considers more than one thickness, have been solved considering pictures from slices having different thicknesses and using a simple algorithm. This produced consistent results[4–6] which were also confirmed by a refinement of the phase separation technique[7]; however, the mathematical procedure needed to solve the system can be additionally improved, because it fails to work in particular cases.

In fact, the algorithm applied to date finds solutions everywhere in the three dimensional space $(\langle R^1\rangle, \langle R^2\rangle, \langle R^3\rangle)$, but, from the physical point of view, not all the values of the unknowns are possible. It is easy to check that the values are physically meaningful provided they satisfy the following relationships:

$$\langle R^1\rangle > 0 \tag{4}$$

and

$$\xi_n = \langle R^n\rangle - \left|(\langle R^{n-1}\rangle)^{\frac{n}{n-1}}\right| \geq 0 \tag{5}$$

for all n greater than 1. It can be noted that ξ_2 coincides with the mean square standard deviation σ^2.

In order to identify acceptable solutions the following method is proposed. We introduce the error function:

$$\begin{aligned} K(\langle R^1\rangle, \langle R^2\rangle, \langle R^3\rangle, \phi) = K_1 + K_2 + K_3 = &\max_i \{|e_i(\langle R^1\rangle, \langle R^2\rangle)|\} \\ &+ \max_i \{|g_i(\langle R^1\rangle, \langle R^2\rangle, \langle R^3\rangle)|\} \\ &+ \max_i \{|h_i(\langle R^2\rangle, \langle R^3\rangle, \phi)|\} \end{aligned} \tag{6}$$

where

$$e_i(\langle R^1\rangle, \langle R^2\rangle) = \left(\langle r_i^1\rangle - \frac{\pi\langle R^2\rangle + 2t_i\langle R^1\rangle}{4\langle R^1\rangle + 2t_i}\right)\frac{1}{\langle R^1\rangle};\ i = 1, 2, \ldots, n \tag{7}$$

$$g_i(\langle R^1\rangle, \langle R^2\rangle, \langle R^3\rangle) = \left(\langle r_i^2\rangle - \frac{4\langle R^3\rangle + 3t_i\langle R^2\rangle}{6\langle R^1\rangle + 3t_i}\right)\frac{1}{\langle R^2\rangle};\ i = 1, 2, \ldots, n \tag{8}$$

$$h_i(\langle R^2\rangle, \langle R^3\rangle, \phi) = \left(\phi_i^{app} - \frac{4\langle R^3\rangle + 3t_i\langle R^2\rangle}{4\langle R^3\rangle}\right)\frac{1}{\phi};\ i = 1, 2, \ldots, n \tag{9}$$

Function K contains linear and normalised error terms (e_i, g_i, h_i) and can be minimised into the space of validity of the solution by simple numerical algorithms. Moreover, all the experimental parameters are taken into account, included ϕ_{app} which, by contrast, was calculated in Ref. 3 only after $\langle R^1\rangle, \langle R^2\rangle, \langle R^3\rangle$ were determined. This route is useful for many reasons: it allows using all the experimental information we have achieved, it is more suitable to compute the errors than the quadratic form because it permits a better definition of the minimum point, and it is more appropriate when one element of the sets: $\{e_1, e_2, \ldots, e_3\}$, $\{g_0, g_2, \ldots, g_3\}$, $\{h_1, h_2, \ldots, h_3\}$, is predominant over the others.

The experimental application of the model followed the procedure described in detail in Ref. 3. The image analysis data for all the materials were, then, utilised as the input data for minimisation of the error function K in its proper mathematical domain.

The search for the minimum point was conducted numerically using the Solver algorithm contained in the widely diffused Microsoft Excel© software and the results are shown in *Table 2*.

Despite the improvement in the mathematical procedure, two values in *Table 2* still appear not to be completely reliable. They are the values of σ for system M3 and the value of ϕ for system E2/10. In the first case the result $\sigma = 0$ would imply that the particle size distribution is monomodal, which seems hard to believe since $f(r)$ appears really broad for the system M3, furthermore there are too many small particle sections close to each other to be cut from different particles with the same radius (*Figure 1*). A reasonable explanation for this incongruence is that the assumption of spherical shape for the particles cannot be considered acceptable in this particular case.

In the second case the following relationship, which must clearly hold for emulsion ABS:

$$\phi_{sep} > \phi \geq \%PB \tag{11}$$

is violated. However, the discrepancy between ϕ and %PB is very low and can easily be ascribed to the experimental error.

Mechanical characterisation

The following experimental techniques were chosen for the investigation of the mechanical behaviour: conventional tensile tests, evaluation of fracture mechanics parameters J and K, dynamic mechanical analysis and TEM observation of plastically deformed thin films.

Tensile tests were performed on all the samples at room temperature and at a cross head speed of 5 mm/min. Dumbbell specimens, machined from compression moulded sheets, were used.

J-testing was performed according to the ESIS protocol[8], making use of a multispecimen procedure[9,10], to measure the J-resistance curves and the fracture toughness $J_{0.2}$ at room temperature. Single edge notch (SEN) specimens, machined from compression moulded sheets, were tested in three-point bending geometry. An Instron dynamometer was used at a cross head speed of 5 mm/min. Two samples were subjected to J-testing for each of the five series investigated, namely samples E1/5, E1/15; E2/5, E2/15; M1/10, M1/20; M2/5, M2/15; M3/5, M3/10. Selection of these samples was based on the tensile modulus: for each series, the modulus of the first sample lay between 3.0 and 3.3 MPa, that of the second one between 2.4 and 2.6 MPa. The reasons for using the tensile modulus as the selection criterion are given in the following. Specimen size was determined according to the testing protocol. Length L, width W, thickness B, span S and the initial notch depth a_0, in mm, were:

$L = 82.0$; $W = 16.0$; $B = 8.0$; $S = 64.0$; $a_0 = 9.0$ for samples E2/15 and M1/20.
$L = 60.0$; $W = 12.5$; $B = 3.2$; $S = 50.0$; $a_0 = 6.9$ for all the other samples.

Fracture toughness K_{Ic} of the pure SAN was evaluated by linear elastic fracture tests according to the 1990 testing protocol approved by ESIS[11]. Specimens, machined from compression moulded sheets, with dimensions $L = 45.0$; $W = 10.0$; $B = 3.2$; $S = 40.0$ and $a_0 = 5.0$ mm, were used.

Dynamic mechanical analysis was carried out on compression moulded specimens by a Rheometrics RSA II in three point bending, with imposed sinusoidal strain (maximum strain = 0.03%) at a frequency of 1 Hz. Test temperature ranged from −120 to −40°C, with a scan rate of 1°/min.

TEM observation of the plastic deformation processes was carried out by means of the in situ copper grid technique described in Ref. 12. Samples with 2.5 vol% of second phase content were prepared by melt mixing with SAN, the amount of which was determined on the basis of the better estimates of the dispersed phase content obtained by the microstructural characterisation. Slices about 1 μm thick were cut by an ultramicrotome and then bonded to copper grids (grids had been previously annealed at 800°C, then dipped into a concentrated SAN solution and dried). The grids were then strained up to 6% strain in uniaxial tension, thus giving rise to plastic deformation of the ABS films. Strained specimens were then directly observed in the TEM.

RESULTS

Figures 2a and *2b* show plots of the tensile modulus E as a function of ϕ_{sep} and ϕ, respectively. Tensile modulus in dispersed-phase systems with spherical particles is known to depend on the total second phase content and on the ratio of the modulus of the particles to that of the continuous phase, but not on the particle size[13]. The modulus of the particles in

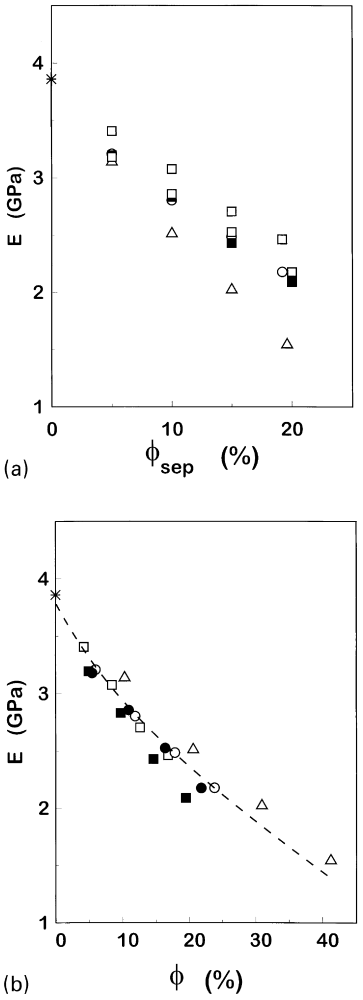

Figure 2 (a) Young's modulus, E, *versus* the second phase volume content measured by means of the standard separation method, ϕ_{sep}. (b) Young's modulus, E, *versus* the second phase volume content measured by means of the image analysis method, ϕ. Symbols relate to materials as follows: ■, E1; ●, E2; □, M1; ○, M2; △, M3; star, SAN. The line is simply a guide for the eye

E samples is that of PB rubber, which, at room temperature, is about 10^3 times smaller than that of SAN. M samples have composite particles with a PB rubber matrix and rigid sub-inclusions: it can be shown, however, that up to a very high sub-inclusion content (more than 95% by volume) the modulus at room temperature of such particles is not significantly different from that of the pure rubber[13]. A single relationship is therefore to be expected between the tensile modulus and the dispersed phase volume content for all the samples considered here. This is actually found in *Figure 2b*. *Figure 2a*, conversely, shows that different relationships are found between E and ϕ_{sep} for each of the samples.

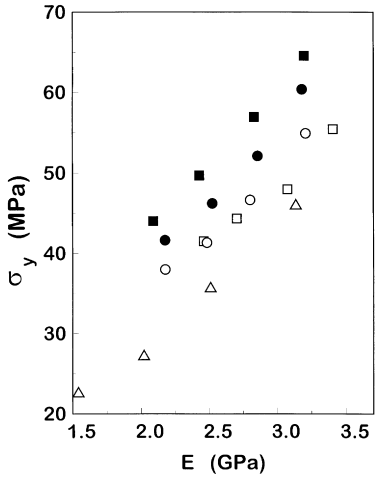

Figure 3 Stress at the yielding point, σ_y *versus* the Young's modulus E: ■, E1; ●, E2; □, M1; ○, M2; △, M3

This supports the validity of the image analysis approach adopted, and the lack of reliability of the separation data, which overestimate the dispersed phase content by including into it the grafted SAN shell surrounding the particles, and, on the other hand, can underestimate the dispersed phase content when part of the sub-included SAN inside the particles is dissolved during the separation process.

The ϕ values obtained by image analysis or, alternatively, the tensile modulus can thus be used as a measure of the rubbery phase content of the samples when comparing their mechanical properties.

Results obtained by the tensile tests are summarised in *Figure 3*. A plot of σ_y *versus* E is shown, which allows the separation of the effects of the morphology from those of the

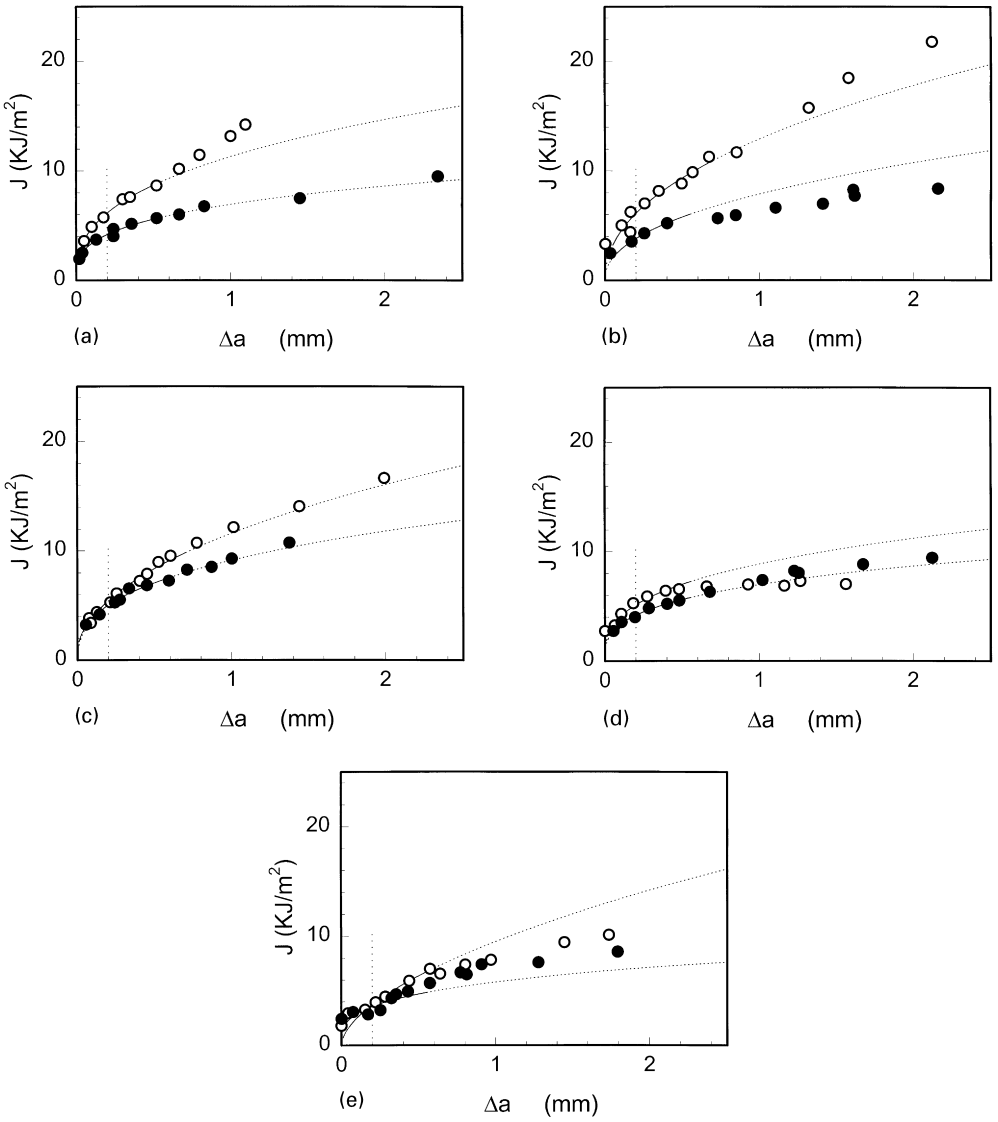

Figure 4 *J*-resistance curves obtained for the samples chosen for *J* testing (see text): (a) E1; (b) E2; (c) M1; (d) M2; (e) M3. Open circles refer to the lower modulus samples, filled circles to the higher modulus ones

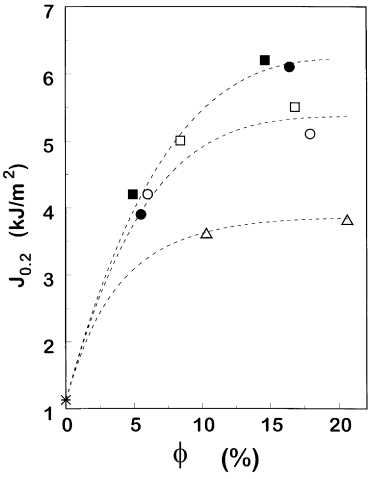

Figure 5 Critical J in mode I, $J_{0.2}$, *versus* the second phase volume content measured by means of the image analysis method, ϕ. ■, E1; ●, E2; □, M1; ○, M2; △, M3 triangles. The K_{1c} value of the pure SAN is shown by the star symbol. The lines are simply guides for the eye

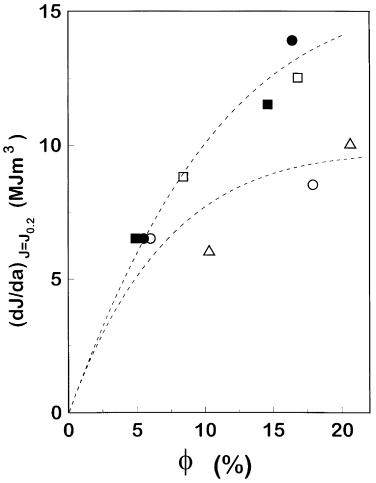

Figure 6 dJ/da computed when $J = J_{0.2}$ *versus* the second phase volume content measured by means of the image analysis method, ϕ. ■, E1; ●, E2; □, M1; ○, M2; △, M3. The lines are simply guides for the eye

dispersed phase content, as discussed above. E-samples have higher yield stress than M-samples at the same ϕ level; E2 (large particles) gives lower yield stress than E1 (small particles) and M3 exhibits the lowest values, while M1 and M2 are comparable. An effect of particle size can therefore be seen, with a possible additional effect of the internal structure of the particles. A qualitative observation has to be reported, concerning the fact that tensile specimens of the E series showed noticeable necking after the yield point, while the M-series ones showed a less localised deformation with a more pronounced stress whitening.

Inspection of the J-resistance curves reported in *Figure 4* shows that E-samples are tougher than M ones, with the possible exception of sample M1. Moreover, a greater toughness increase with increasing rubbery phase content is observed for the emulsion made materials. *Figure 5* reports the $J_{0.2}$ values, measured at a crack advancement equal to 0.2 mm according to the ESIS protocol, plotted against the rubbery phase content: higher toughness, particularly at the higher ϕ levels, is found for the emulsion-polymerised materials. When (dJ/da) is considered (*Figure 6*), sample M1 appears to be comparable to the E-samples, whereas M2 and M3 exhibit lower values.

Dynamic mechanical behaviour in the temperature range corresponding to the glass transition of the rubber, reported in *Figure 7* by plots of tan δ *versus* temperature, shows that the rigid sub-inclusion content has a definite influence on the stress field existing inside the particles and in the matrix immediately surrounding them. The tan δ peak temperature, which can be considered as representative of the glass transition temperature T_g of the rubber, is not affected by the rubbery phase content in the M2 series (the behaviour of M1 and M3 is similar), while in both the E series it shifts to lower values as the rubbery phase content is decreased. In the large-particle emulsion series E2, moreover, a splitting of the peak into two smaller ones is observed at the lowest rubbery phase content.

Similar features in the loss peaks of emulsion-made ABS materials were observed by Morbitzer *et al.*[14], who ascribed the peak shift to the thermal stress arising inside the rubber due to the thermal expansion mismatch between the rubber and the surrounding matrix. When the material is cooled below the glass transition temperature of SAN, the rubber, which has the higher thermal expansion coefficient, undergoes a hydrostatic dilatation stress. This stress is higher for lower rubbery phase contents because the relevant thermal expansion mismatch is actually that existing between the rubber inside each particle and the surrounding two-phase material as a whole, whose expansion coefficient is intermediate between those of pure rubber and pure SAN and dependent on the rubbery phase content. Peak splitting phenomena were also observed by the above mentioned authors in some materials at low temperatures and low rubbery phase contents and were interpreted on the basis of mechanical failure occurring at the matrix–rubber interface or inside the rubber under the action of the thermal stress. Rubber particles involved in such failure phenomena are no more subjected to the dilatation stress, and their contribution to the T_g peak is shifted back to a higher temperature, corresponding to the T_g of the unstressed rubber.

Thermal stresses have been calculated by Pavan and Riccò[15] for a model system in which a composite particle containing a single spherical rigid sub-inclusion is surrounded by a rigid matrix. It was shown that the thermal stress, which is maximum for a pure rubber particle with no sub-inclusion, is strongly decreased as the volume fraction of the particle occupied by the sub-inclusion increases.

Dynamic mechanical data in *Figure 7* can then be interpreted on the basis of these considerations. The large sub-inclusion content in M-samples prevents the build up of thermal stresses, which are instead present in the E-samples: this accounts for the lack of peak shifts in the first case and for the shifts observed in series E1 and E2. Peak splitting, which is observed for E2 but not for E1, might be due to a weaker interfacial adhesion in the large particle sample, or to a higher occurrence, in the same sample, of cavitation phenomena inside the rubber particles under the action of the strong thermal stress existing at the low temperatures reached during the tests.

The local elastic stress field inside the dispersed particles and in the surrounding matrix is therefore affected by the internal structure of the particles.

Relationships between the observed macroscopic mechanical behaviour and the plastic deformation micromechanisms may be analysed by considering the results of

the 'copper grid' experiments. *Figures 8–14* show the main features observed on the different samples. They can be summarised as follows.

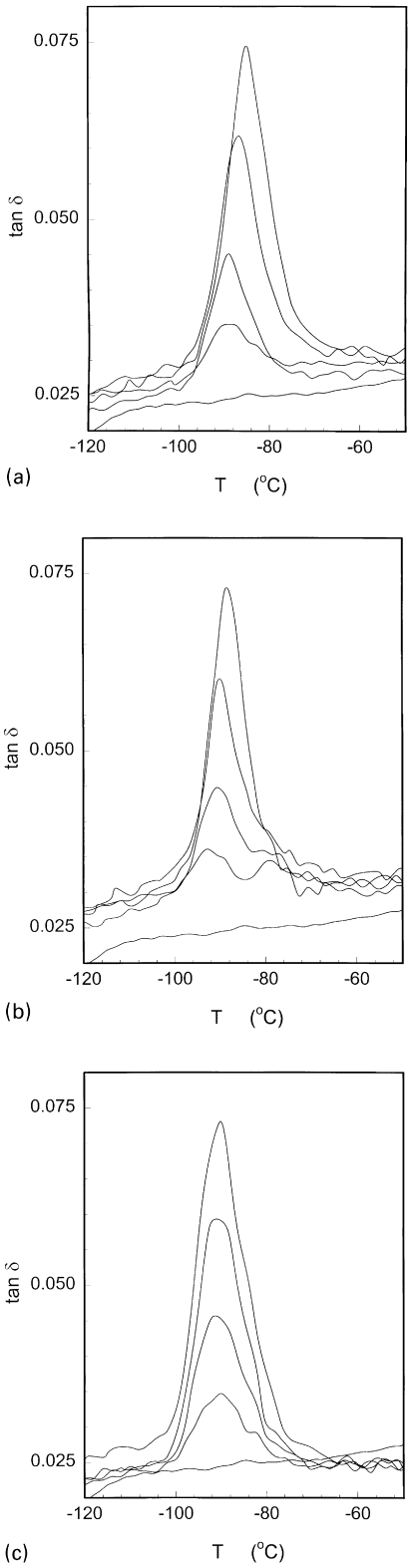

Figure 7 (a) Tan δ *versus* temperature, *T*, for material E1. The curves are relative to materials having ϕ values of 0, 5, 10, 15 and 20%, respectively, going from the lowest to the highest. (b) Tan δ *versus* temperature, *T*, for material E2. The curves are relative to materials having ϕ values of 0, 5, 10, 15, 20%, respectively, going from the lowest to the highest. (c) Tan δ *versus* temperature, *T*, for material M2. The curves are relative to materials having ϕ values of 0, 5, 10, 15 and 24.4%, respectively, going from the lowest to the highest

(1) In emulsion-made samples E1 and E2 (*Figures 8* and *9*) only the largest particles appear to be active as craze nucleation sites. A large number of particles which are not associated with crazes can be observed.
(2) Evidence of shear deformation phenomena in samples E1 and E2 is given by the presence of diffuse-shear zones in sample E2 (the lighter-contrast region marked by 'B' in *Figure 9*) and by the association of crazes in band-like structures, which were observed most frequently in sample E1, as the image in *Figure 14* shows. In all cases the shear zones and the heavily crazed bands are inclined at approximately 45° with respect to the applied stress direction (labelled by A-A in the figures).
(3) Cavitation of the rubber particles was observed in sample E2. Evidence for that can be found in *Figure 9* (relevant spots are marked by 'C'); a typical cavitated particle is shown at higher magnification in *Figure 13*.
(4) Mass polymerised materials gave little evidence of shear deformation. In M1 only (*Figure 10*) some band-like structures formed by the crazes were observed, with about the same inclination with respect to the applied stress direction as that of the heavily crazed bands in sample E1 (*Figure 14*).
(5) In M2 and M3 samples (*Figures 11* and *12*, respectively) no evidence for deformation micromechanisms other than crazing is observed. Crazes are nucleated by the rubber particles and grow in planes which are

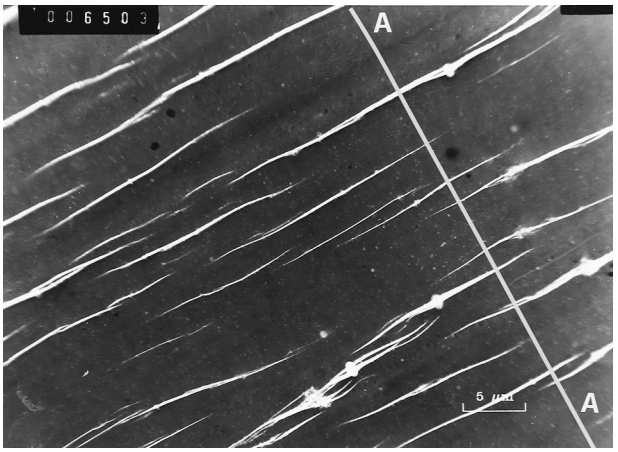

Figure 8 TEM micrograph of sample E1/2.5 after plastic deformation

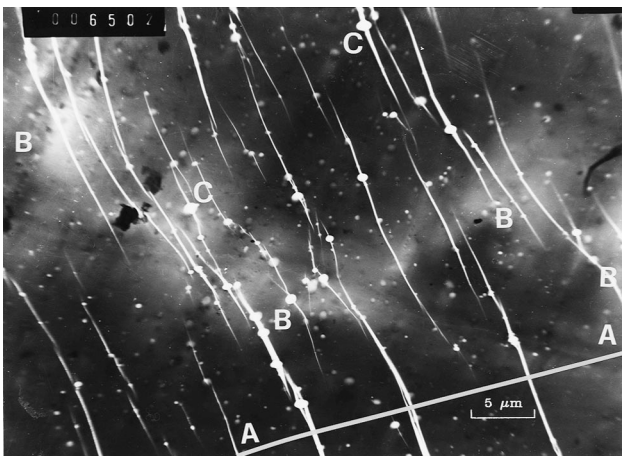

Figure 9 TEM micrograph of sample E2/2.5 after plastic deformation

perpendicular to the applied stress direction (A-A). Craze dimensions and density (number of crazes observed per unit surface of microtomed slice) appear to be related to the size and size distribution of the rubber particles: sample M2 shows a relatively homogeneous distribution of crazes similar in size and shape, while in sample M3 fewer crazes of varying size may be observed.

DISCUSSION

The mechanical behaviour of E-samples, which exhibit higher yield stress and higher fracture toughness at a given rubbery phase content, seems to indicate that particles coming from the emulsion process, which have much lower sub-inclusion content and generally smaller dimensions than mass polymerised particles, have a better toughening efficiency in ABS systems. Some differences in the plastic deformation mechanisms associated with the different particle structures and morphologies may therefore be expected.

TEM images of plastically deformed films obtained by the copper grid technique (*Figures 8–14*) actually confirm this: evidence of shear deformation can mostly be found in emulsion-polymerised samples, while the mass polymerised ones appear to deform almost exclusively by crazing. Sample M1 only, within the M-series, shows some features in the arrangement of crazes (see *Figure 10*), which may be interpreted as the result of shear deformation processes. Diffuse shear was observed only in sample E2, which is also the only one in which cavitation of the rubber particles was detected after cooling at low temperatures in dynamic mechanical experiments and after plastic deformation in the thin films observed by TEM.

A first point to be taken into account for the interpretation of these results is the existence of a critical particle size, below which the craze nucleation ability of the particles is strongly reduced. This has been shown to be true in the case of HIPS[16–18], and was explained by assuming that the stress concentration field around the particles, whose intensity and shape do not depend on the particle size, must extend over a minimum distance from the particle's surface in order to be effective for craze nucleation. The critical particle size for HIPS has been reported to be about 1 μm[18], a value which can of course be different in the case of ABS. It is reasonable to admit, however, that a definite critical value exists for ABS and that, therefore, too small particles are not effective as craze nucleation sites in these materials.

An interpretation of the fact that multiple crazing appears to occur more extensively in M-samples than in E-samples may thus be based simply on the generally smaller particle size of the emulsion-made materials.

The effects of particle size on crazing cannot however account for all the differences observed in the mechanical

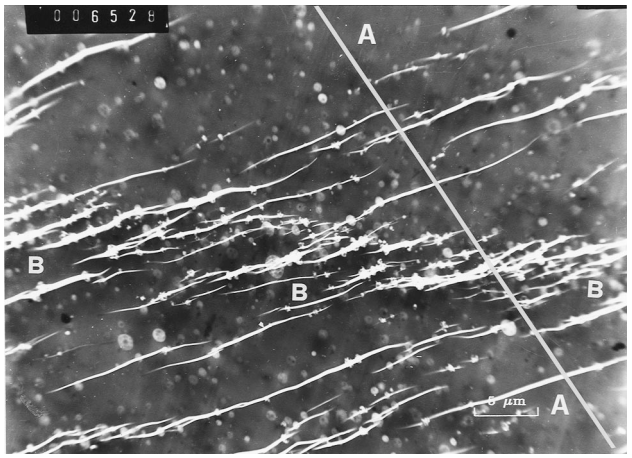

Figure 10 TEM micrograph of sample M1/2.5 after plastic deformation

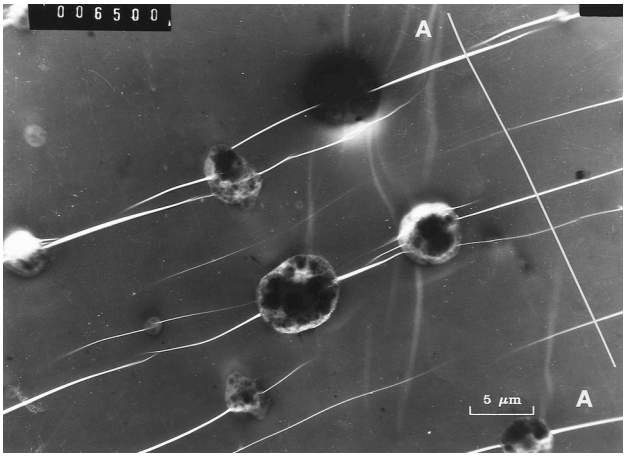

Figure 12 TEM micrograph of sample M3/2.5 after plastic deformation

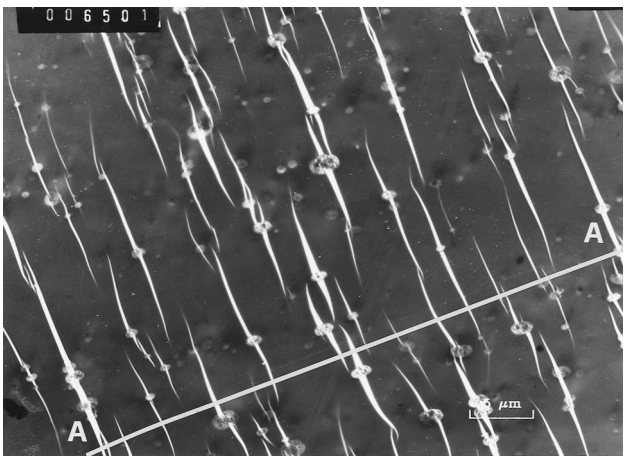

Figure 11 TEM micrograph of sample M2/2.5 after plastic deformation

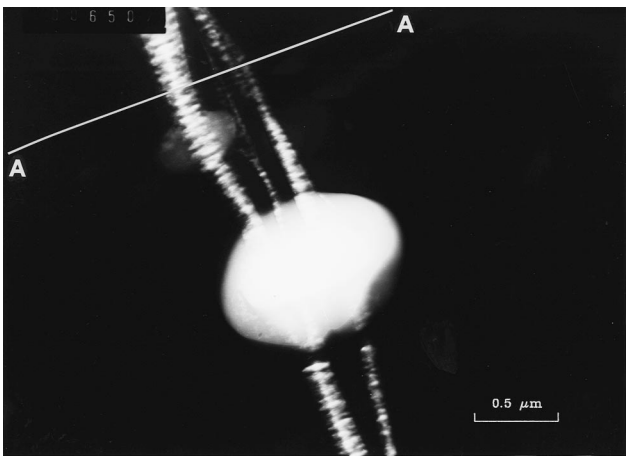

Figure 13 A cavitated rubber particle in sample E2/2.5 after deformation

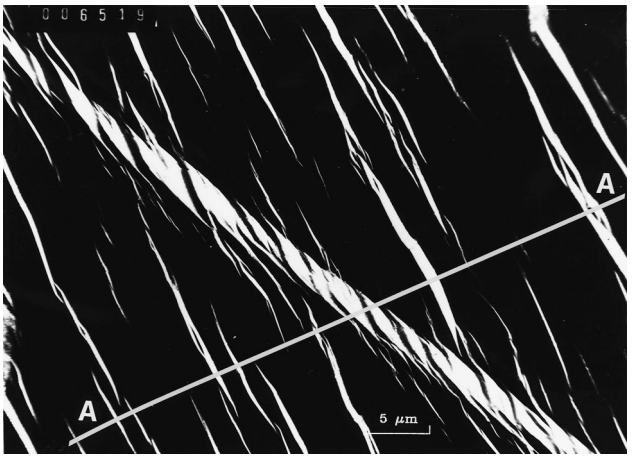

Figure 14 Association of crazes in band-like structures in sample E1/2.5 after deformation

behaviour of our samples. The high fracture toughness of the small particle materials (samples E1, E2 and M1), reveals that in these samples better energy dissipation mechanisms are active than in M2 and M3, despite the partial suppression of the multiple crazing mechanism due to the small particle size distribution. As the copper grid results show, these energy dissipation mechanisms are to be related to the presence of shear deformation processes, which therefore are to be taken into account when considering the toughening effects of the small particles.

Basically two different shear deformation processes have been observed, as reported above: diffuse shear, found only in sample E2 together with cavitated particles, and the association of crazes in bands, inclined with respect to the applied stress direction, observed in E1 and M1.

The importance of cavitation in rubber toughening, particularly with reference to the shear deformation of the matrix, has been stressed by several authors[19–21]. Cavitation of the rubber particles has been shown to take place before plastic deformation of the matrix, not only when the matrix is ductile, but even for HIPS, in which the dominant deformation mechanism of the PS continuous phase is crazing. Ductile deformation of the matrix material ahead of a crack has been shown to be enhanced by cavitation, e.g. in Nylon 6–rubber blends[20,21]. An explanation of this has been given by considering that particle cavitation leads to the relief of the triaxial stress ahead of a crack, thus increasing the size of the plastic zone.

A model which allows a quantitative assessment of the conditions for cavitation has been developed by Bucknall *et al.*[22,23]. Main parameters which determine the cavitation inside a rubber particle are the overall volume strain, the particle's size, the shear modulus of the rubber, its surface tension and its failure strain. A critical particle size exists, at fixed values of the other parameters, below which cavitation cannot occur.

The toughening efficiency of particles which are too small for craze nucleation may therefore be connected with their cavitation occurring under the triaxial stress state existing at the crack tip during fracture. According to the above reported interpretations, cavitation should induce diffuse shear deformation of the matrix, and this is indeed observed in the case of sample E2. Again, the existence of a critical size has to be expected, the value of which depends on the overall volume strain and on the properties of the rubber.

As far as the volume strain is concerned, consideration has to be given to the presence of the above discussed thermal expansion mismatch between matrix and rubber, which was shown to be strongly affected by the particles' sub-inclusion content. The resulting stress state is a purely hydrostatic dilatation inside the rubber, and can thus give a positive contribution to the volume strain of the particles subjected to an externally applied stress. The critical applied stress for cavitation can therefore be expected to be lower for the bulk rubber particles than for the 'salami' particles, if all the other conditions (applied stress, particles size, etc.) are the same.

On the basis of these considerations some interpretation can be proposed for the experimental results concerning samples E1, E2 and M1.

Plastic deformation in sample E2 may be described as occurring by cavitation of the rubber particles followed by shear deformation of the matrix.

In the case of sample E1 this deformation process is hindered because of the small size of the particles: as the quoted model shows, values for the critical particle diameter, below which cavitation does not occur, may generally be expected to be of the order of 0.1 μm, which is actually very near to the average size of E1 particles.

As far as sample M1 is concerned, a reduced thermal stress exists inside the particles because of the high sub-inclusion content, and this can result in too low volume strain under the deformation conditions imposed during the copper grid experiments to induce cavitation of the particles.

Samples E1 and M1 nevertheless exhibit fairly good mechanical behaviour, which may be explained by considering the observed simultaneous occurrence of crazing and shear deformation within the heavily crazed bands as described above.

As recently proposed by Lazzeri and Bucknall[22], the presence of voids in a ductile matrix affects the pressure dependence of the yield stress so that the yield condition is reached well before the macroscopic equivalent stress equals the matrix flow stress. These considerations are the basis of the proposed formation of the 'dilatation bands' which are the result of the association of cavities (cavitated particles) and shear bands. We did not observe such dilatation bands (cavitated particles arranged in an inclined direction with respect to the applied tensile stress) in our copper grid experiments, but we had evidence of analogous arrangement of crazes in samples E1 and M1. As pointed out above, in these two samples the critical stress for particle cavitation can be higher than in sample E2, because of too small a particle size in E1 and of a too high sub-inclusion content (low thermal stress) in M1. This could restrain the shear deformation of the matrix and encourage the concurrent mechanism of multiple crazing, in analogy with the case of samples M2 and M3. Particles in E1 and in M1 are however too small for an extensive diffusion of crazing throughout the material, and the comparatively small crazes which result may act as voids, arranging in the observed heavily crazed bands where a simultaneous shear deformation can take place. This could be a qualitative explanation for the good fracture toughness of samples E1 and M1.

ACKNOWLEDGEMENTS

EniChem is gratefully acknowledged for the supply of the materials and for the availability of the equipment. M. Merlotti, S. Simonazzi and M. Vighi are thanked for the assistance in performing the microscopic analysis. The authors are grateful to K. Pisoni for her kindness and valued collaboration in carrying out the mechanical characterisations.

REFERENCES

1. Keskkula, H. and Pratt, A. E., in *Encyclopaedia of Polymer Science and Technology*, Vol 13. John Wiley, New York, 1970.
2. Cigna, G. J., *Appl. Polym. Sci.*, 1970, **14**, 1781.
3. Maestrini, C., Merlotti, M., Vighi, M. and Malaguti, E., *J. Mater. Sci.*, 1992, **27**, 5994.
4. Maestrini, C., Monti, L. and Kausch, H. H., *Polymer*, 1996, **37**, 1607.
5. Maestrini, C., Pisoni, K. and Kausch, H. H., *J. Mater. Sci.*, 1996, **31**, 3249.
6. Maestrini, C., Callaioli, A., Rossi, M. and Bertani, R., *J. Mater. Sci.*, 1996, **31**, 3747.
7. Anzaldi, S., Bonifaci, L., Malaguti, E., Vighi, M. and Ravanetti, G. P., *J. Mater. Sci. Lett.*, 1994, **13**, 1555.
8. ESIS (European Structural Integrity Society), *Recommendation for Determining the Fracture Resistance of Ductile Materials*, 1991.
9. Huang, D. D., *ASTM STP*, 1991, **1114**, 290.
10. Hale, G. E., *Proc. 8th Int. Conf Def. Yield Fracture Polym*., Cambridge, Plastics and Rubber Institute, London, 1991.
11. ESIS, *A Linear Elastic Fracture Mechanics (LEFM) standard for determining Kc and Gc for plastics*, 1990.
12. Lauterwasser, B. D. and Kramer, E. J., *Phil. Mag.*, 1979, **A39**, 469.
13. Nielsen, L. E., in *Predicting the Properties of Mixtures.* Marcel Dekker Inc., New York, 1978.
14. Morbitzer, L., Kranz, D., Humme, G. and Ott, K. H., *J. Appl. Polym. Sci.*, 1976, **20**, 2691.
15. Pavan, A. and Riccò, T., *J. Mat. Sci., Lett.* , 1976, **11**, 1180.
16. Bucknall, C. B., *Toughened Plastics*. Applied Science, London, 1977.
17. Bucknall, C. B., in *Polymer Blends*, ed. D. R. Paul and S. Newman. Academic Science, New York, 1978.
18. Donald, A. M. and Kramer, E. J., *J. Appl. Polym. Sci*., 1982, **27**, 3729.
19. Bucknall, C. B., Heather, P. S. and Lazzeri, A., *J. Mater. Sci.*, 1989, **16**, 2255.
20. Borggreve, R. J. M., *Polymer*, 1989, **30**, 71.
21. Dijkstra, K., Van Der Wal, A. and Gaymans, R. J., *J. Mater. Sci.*, 1994, **29**, 3489.
22. Lazzeri, A. and Bucknall, C. B., *J. Mat. Sci.*, 1993, **28**, 6799.
23. Bucknall, C. B., Karpodinis, A. and Zhang, X. C., *J. Mat. Sci.*, 1994, **29**, 3377.